

Moving Vessel ADCP Measurement of Tidal Streamfunction using Radial Basis Functions -PREPRINT 2006

Ross Vennell

Department of Marine Science, University of Otago, New Zealand

Rick Beatson

Department of Mathematics and Statistics, University of Canterbury, New Zealand

Abstract. Acoustic Doppler Current Profiler measurements from moving vessels have recently been used to obtain detailed observations of the spatial patterns of tidal flows, as well as patterns of vorticity and dynamical terms. Developments in Radial Basis Function interpolation theory are demonstrated to significantly improve the quality of the tidal velocity field extracted from the measurements using thin plate splines. These include placing centers at data locations, enforcing “side conditions” on the solution and using higher order splines. For tidal flows with a scale less than a few kilometers, the differentiability of RBFs can be exploited to fit the streamfunction directly to the measurements. This ensures the observed tidal velocity field satisfies mass continuity. Enforcing mass continuity is demonstrated to significantly improve the ability of the splines to interpolate across wide gaps between vessel tracks. Extraordinarily detailed ADCP measurements of the tidal streamfunction within Bluff Harbour, NZ, reveal the stagnation streamline which separates a 200m wide flood tidal jet from an associated 400m diameter eddy. The stagnation streamline clearly shows that the eddy gains its fluid and vorticity from inshore of the jet’s vorticity maximum. The eddy forms at 04:45 hours before high tide, grows in spiral fashion, and becomes isolated from the jet 02:30 hours before high tide, after which its vorticity rapidly decays.

1. Introduction

Moving vessel ADCP (MV-ADCP) measurements have the potential not only to yield the detailed spatial patterns of tidal currents, but also patterns of vorticity and dynamical terms. For example *Geyer and Signell* [1990] give observations of the spatial structure and development of a tidal headland eddy and *Simpson et al.* [1990] a vertical cross-section of tidal flow in a channel. Exploiting improved ADCP technology, *Old and Vennell* [2001] achieved 100m horizontal resolution for the velocities within an ebb tidal jet and were able to compare its growth, through entrainment of surrounding water, with classical plane jet theory. These observational works improve the understanding of the dynamics of the coastal ocean either directly or as verification for theoretical or numerical models. *Vennell* [2006] presented MV-ADCP measurements in a constricted tidal channel of the 2D spatial pattern of the advection and bottom friction terms in the depth averaged momentum equation with a 60m resolution. He also gave ADCP measurements of the free surface, i.e. the “dynamical topography”, found by inverting the momentum equation. The ADCP measurements showed that advection dominated the momentum balance in the channel, that the free surface was depressed by 7cm in the highest flow region and that bottom friction resulted in a 2cm head loss over 500m. The measurements provided observational support for the numerical modeling results of *Hench and Luettich* [2003].

The above observational works used repeated circuit MV-ADCP measurements, in which a vessel steams around the same track multiple times during a complete tidal cycle. These measurements contain information about both the

spatial and temporal variability of the tidal currents within the area covered by the circuit. The measurements also have high spatial resolution along the vessel track, but there are often wide gaps between vessel tracks, requiring interpolation between tracks, e.g. *Geyer and Signell* [1990].

To separate spatial and temporal components of the flow in MV-ADCP measurements *Geyer and Signell* [1990], *Simpson et al.* [1990] and *Vennell* [1994] spatially binned measurements from each circuit. The time series of velocities for each bin was analyzed using conventional tidal analysis techniques to yield tidal current harmonic coefficients for the bins [*Godin*, 1972]. The spatial binning technique is simple to implement, however tidal analysis in adjacent bins is carried out independently, which may lead to spatially noisy coefficients. *Candela et al.* [1992] used 2D Thin Plate Splines (TPS) to more smoothly represent the spatial structure of tidal currents. Two dimensional TPS are physically equivalent to placing weights on a thin plate, bending it to fit the heights given by the data. *Muenchow* [2000] extended *Candela et al.*’s technique to 3D TPS to obtain 3D velocity structure on the New England Shelf from a combination of MV-ADCP and moored current meter measurements. The small data sets of *Candela et al.* and *Muenchow* allowed only a small number of weights to be used and both found that their TPS velocity fields were sensitive to the number and location of the weights.

For denser data sets *Vennell* [2006] showed that, provided the vessel tracks were sufficiently close, and there are sufficient weights to resolve the smallest spatial scale of interest, tidal velocity fields found using TPS are insensitive to the number and location of the weights. For example, to resolve a feature 10% of the size of the measurement area $\mathcal{O}(100)$ weights are needed. *Vennell* also showed that with too many weights the results became worse due to buckling of the TPS surface between data locations. *Vennell*’s work did not explore where best to place the weights and indicated only an

order of magnitude for the number of weights required to achieve insensitivity. His work used too many weights and employed singular value editing to smooth spline buckling.

The TPS used by *Candela et al.* are one class of Radial Basis Functions (RBFs). RBFs are functions which can be expressed in terms the radial distance from a given center. Typically there are many centers (called nodes by *Candela et al.*), so that RBFs can approximate any continuous function. RBFs can be used to represent functions in one or more dimensions, but we will consider only 2D TPS RBFs in this paper. TPS RBFs have the property of giving the smoothest interpolating surface, as they have minimum linearized curvature or plate energy (see for example *Beatson et al.* [2004]). This smoothness makes them ideal for interpolating across wide gaps in the data, such as those between vessel tracks.

The aims of this paper are to improve the tidal velocity field extracted from noisy MV-ADCP measurements and to enable clear delineation of flow structures within the field. To do this we exploit developments in RBF techniques, demonstrate their adaptation and extension to repeated circuit MV-ADCP data and develop a technique to fit the streamfunction to the velocity measurements. The objective is to thoroughly develop and test the technique as the basis for future uses in coastal observational oceanography. Section 2 summarizes some relevant results from the RBF literature. Section 3 gives extensions to the RBF techniques and tests them with synthetic data. Section 4 shows how to fit the streamfunction to velocity measurements. The tidal MV-ADCP works mentioned above fitted the velocity components independently. Fitting the streamfunction ensures the components of the predicted velocity field satisfy conservation of mass. It is demonstrated that this physical constraint can significantly improve the velocity field derived from MV-ADCP measurements. Fitting the streamfunction also has the advantage of being able to easily identify important streamlines within the tidal flow, such as the stagnation streamline which delineates an eddy from its associated tidal jet. In section 5 we demonstrate the results obtainable from the RBF tidal analysis of MV-ADCP measurements of a real flood tidal jet and its associated eddy.

2. RBF interpolation

TPS are a mathematical model for the displacement of a thin plate which has been constrained to pass through certain points given by the data. A TPS interpolant minimizes a linearization of the plate's bending energy. Algorithmically this involves placing particular radially symmetric functions, basic functions, at prescribed locations or "centers", choosing the weights to fit the functional surface to the data. 2D interpolation seeks a functional surface passing through every data point which can be evaluated between data locations. Thus for RBF interpolation there must be as many centers as data points. The focus of this work is a smoother RBF surface which is the best representation of noisy data in a least squares sense. This is done by having fewer centers than data points and consequently this smoother surface may not pass through any data point. To obtain this smoother surface we exploit ideas from RBF interpolation theory. The standard setting for RBF interpolation is a set of functions F for which there is a quadratic functional which can be interpreted as a measure of its smoothness, or energy [*Beatson et al.*, 2004]. For example for 2D biharmonic TPS the associated measure of energy is

$$E(F) = \int_{\mathcal{R}^2} \left(\frac{\partial^2 F}{\partial x^2} \right)^2 + 2 \left(\frac{\partial^2 F}{\partial x \partial y} \right)^2 + \left(\frac{\partial^2 F}{\partial y^2} \right)^2 dx dy, \quad (1)$$

where \mathcal{R}^2 is all of 2D space. It can be shown that for a measure of smoothness of the form (1), and under weak conditions on the geometry of the centers, the unique smoothest interpolant is an RBF, i.e. a function of the form

$$S(\mathbf{x}) = P(\mathbf{x}) + \sum_{n=1}^N \lambda_n \Phi(|\mathbf{x} - \mathbf{y}_n|), \quad (2)$$

where Φ is a fixed function, $\{\mathbf{y}_n\}$ are location vectors of the N RBF centers and P is a polynomial of degree K . In this paper bold face \mathbf{x} and \mathbf{y} are vectors with components x and y . The $\Phi(|\mathbf{x} - \mathbf{y}_n|)$ term in (2) depends only on the distance $|\mathbf{x} - \mathbf{y}_n|$ between the location \mathbf{x} and the center \mathbf{y}_n . As a function of \mathbf{x} , the shifted basic function $\Phi(|\mathbf{x} - \mathbf{y}_n|)$ is radially symmetric about \mathbf{y}_n . Equation (2) is rewritten more explicitly in equation (14) of the appendix. The RBF weights λ_n must satisfy the side conditions

$$\sum_{n=1}^N \lambda_n p(\mathbf{y}_n) = 0, \quad (3)$$

for all polynomials p of degree K or less. For example, for a 2D linear polynomial, $K = 1$, (3) must hold separately for $p = 1$, $p = x$, and $p = y$. Equation (13) in the appendix gives an example of these side conditions in matrix form. The side conditions (3) have the effect of constraining the growth of the RBF as $|\mathbf{x}| \rightarrow \infty$, and localizing the energy of the RBF to regions near the centers. To be the smoothest interpolating function passing through every data point, centers must be placed at every data location i.e. the N center locations, $\{\mathbf{y}_n\}$, are the same as the L data locations, $\{\mathbf{x}_n\}$ and N must equal L .

One class of RBFs (2) are the TPS. The lowest order continuous TPS in \mathcal{R}^2 are the biharmonic TPS for which the basic function Φ in (2) is a multiple of the Green's function, or fundamental solution, of $\nabla^4 f(\mathbf{x}) = g(\mathbf{x})$. In 2D the basic function is $\Phi(\mathbf{x}) = |\mathbf{x}|^2 \log |\mathbf{x}|$, the polynomial P in (2) is linear ($p = 1$, x or y) and the condition on the geometry of the centers is that they do not all lie on a single straight line. This condition ensures that the side conditions (3) are linearly independent. Taking the limit as $\mathbf{x} \rightarrow 0$ using L'Hôpital's rule shows that the basic function, $\Phi(\mathbf{x}) = |\mathbf{x}|^2 \log |\mathbf{x}|$, is zero at 0. Consequently the biharmonic TPS is continuous everywhere. The biharmonic's first derivatives are also continuous everywhere. It is this continuity in first derivatives which gives TPS their visual smoothness. However second and higher derivatives of biharmonic TPS are not continuous. The next highest order TPS are the triharmonic TPS. In 2D the corresponding basic function is $\Phi(\mathbf{x}) = |\mathbf{x}|^4 \log |\mathbf{x}|$, the polynomial P is quadratic ($p = 1$, x , y , x^2 , xy or y^2) and its measure of energy has third derivatives in the integrand of (1). The smoother triharmonic TPS have continuity up to and including their third derivatives.

There are many consequences of the smoothest interpolant property of (2). In particular the uniqueness implies that any other interpolant has higher energy. This includes interpolants of the same form as (2) where some of the centers of the RBF are not located at the data locations. This argues very strongly for using data locations as the centers of an interpolating RBF. Furthermore, the side conditions (3) are necessary for (2) to be the smoothest interpolant. Indeed in many cases, including biharmonic and triharmonic TPS, far field expansions show that the energy integrals of the form (1) are infinite if the RBF does not satisfy the corresponding side conditions (3).

In this paper the focus is on data with significant noise and we seek a smoother RBF surface which best represents the data in a least squares sense by using few centers than data points. Currently there is no theory to support an RBF as the smoothest surface for this least squares fit, however smoothest interpolation theory motivates us for a least squares RBF to

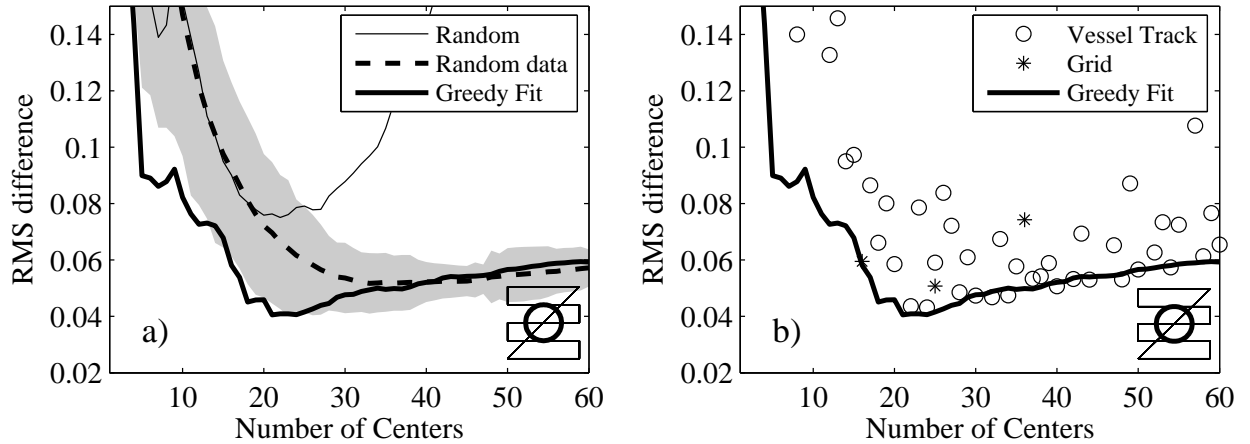


Figure 1. Comparison of center selection schemes for biharmonic Thin Plate Spline RBF fit to a synthetic eddy. a) Average RMS difference between fit predictions and Gaussian eddy for 50 sets of randomly located centers (thin solid line) and randomly selected data point centers (thick dashed line). The gray area gives the replicate variability interval (RVI) for the 50 sets of randomly selected data point centers. The thick solid line is RMS difference for a single “greedy fit”. The inset shows the vessel track and eddy location. b) RMS differences for centers evenly spaced along the vessel track (circles) and evenly gridded centers (stars). Thick solid line is the greedy fit.

1. Place the centers at data locations.
2. Require that the side conditions be satisfied in order that the fit has finite energy.

Tests supporting these choices are given below. The RBF interpolation literature is huge and *Beatson et al.* [2004] and *Meinguet* [1979] cover much of the theory in an applications motivated manner for the non-specialist.

To obtain the RBF weights and polynomial’s coefficients the overdetermined set of equations which result from using a function of the form (2) to approximate the observations in the least squares sense is solved. The system has the form

$$\mathbf{D}\mathbf{w} \approx [\mathbf{d}] \quad \text{where } \mathbf{D} = [\mathbf{A} \quad \mathbf{P}] \quad (4)$$

Here \mathbf{D} is the least squares “design matrix”, \mathbf{d} is the vector of the measured surface heights and $\mathbf{w} = [\lambda; \beta]$ is the vector of RBF weights, made up of the coefficients λ_j of the shifts of $\Phi(\mathbf{x})$ and polynomial coefficients β_j . Let $\mathbf{x}_1^d, \dots, \mathbf{x}_L^d$ be the measurement locations, $\mathbf{y}_1, \dots, \mathbf{y}_N$ be the RBF centers, and $\{p_k\}$ be a basis for the polynomial space, e.g. the functions $\{1, x, y\}$ for linear polynomials in 2D. Then $\mathbf{A}_{ij} = \Phi(|\mathbf{x}_i^d - \mathbf{y}_j|)$, the polynomial P in (2) is $P(\mathbf{x}) = \sum_k \beta_k p_k(\mathbf{x})$, and $\mathbf{P}_{ik} = p_k(\mathbf{x}_i^d)$. Equations (12) and (13) in the appendix detail the entries in the design matrix and the constraint equations. For a linear polynomial in 2D the design matrix, \mathbf{D} , is L by $N + 3$ in size and for the work presented here it is heavily over determined, with an order of magnitude more rows than columns. Using many fewer centers than data points results in both a smoother and a computationally more tractable fit. Once (4) is solved for the coefficients \mathbf{w} the surface height can be evaluated at any location vector \mathbf{x} using (2).

To obtain a fitted surface with finite energy, we solved the over determined rectangular set of equations (4) subject to the side conditions (3) as linear equality constraints on the least squares solution. The computation was performed using the null space method and QR factorization (see for example *Bjorck* [1996]). The constraints do not add additional parameters but are conditions the RBF weights must meet. Constrained least squares solution algorithms are part of public domain numerical software libraries such as LAPACK. LAPACK routines are available in FORTRAN and C, and are incorporated into MatLab.

3. RBF Tidal analysis

Extending the RBF representation to allow for tidal variation, we use (2) to represent the spatial structure of the tidal current harmonic coefficients. In mathematical terms our approximation is the tensor product of an RBF for the spatial variation with a trigonometric function for the time variation. More explicitly, the horizontal components of tidal velocity, $(u(\mathbf{x}, t), v(\mathbf{x}, t))$, are represented as

$$\begin{aligned} u(\mathbf{x}, t) &= F_0^u(\mathbf{x}) + \sum_{m=1}^M [F_m^u(\mathbf{x}) \cos(\omega_m t) \\ &\quad + G_m^u(\mathbf{x}) \sin(\omega_m t)], \\ v(\mathbf{x}, t) &= F_0^v(\mathbf{x}) + \sum_{m=1}^M [F_m^v(\mathbf{x}) \cos(\omega_m t) \\ &\quad + G_m^v(\mathbf{x}) \sin(\omega_m t)]. \end{aligned} \quad (5)$$

Here all the functions $F(\mathbf{x})$ and $G(\mathbf{x})$ are RBFs of the form (2) and the ω_m ’s are the tidal frequencies included in the tidal analysis. The F ’s and G ’s have exactly the same functional form as they use the same centers and differ only in the values of their RBF and polynomial coefficients, with different coefficients for each choice of sub and superscript. Equation (5) is the same as *Candela et al.*’s velocity expansion except for the polynomial terms and the enforcement of the side conditions on the fit. An indicial form of (5) is given in the appendix as (15). Each velocity component fitted with (5) using a linear polynomial requires the $(N + 3)(2M + 1)$ coefficients within \mathbf{w} to be found by fitting (5) to the L MV-ADCP data values while enforcing the $3(2M + 1)$ side conditions in (3). The tidal least squares design matrix has the same form as (4), with the \mathbf{A} and \mathbf{P} matrices augmented on the right with $2M$ copies of themselves multiplied by either $\sin(\omega_m t)$ or $\cos(\omega_m t)$ evaluated at the measurement times i.e.

$$\mathbf{D}^{tidal} = [\mathbf{D} \quad \mathbf{D} \sin(\omega_1 t) \quad \mathbf{D} \cos(\omega_1 t) \quad \dots] \quad (6)$$

and the tidal coefficient vector $\mathbf{w}^{tidal} = [\mathbf{w}_0; \mathbf{w}_{S1}; \mathbf{w}_{C1}; \dots]$ solves $\mathbf{D}^{tidal} \mathbf{w}^{tidal} = [\mathbf{u}^d \text{ or } \mathbf{v}^d]$.

3.1. Synthetic data

Synthetic MV-ADCP data sets are used to test the performance of RBF tidal analysis (5). The synthetic vessel track lay within a unit square, with the lower left corner at the origin. The tracks were either on lines parallel to the x axis spaced 0.2 unit intervals or around the perimeter of the unit square. The track was repeated 10 times during a single tidal cycle, with 900 data points 0.2 units apart. The synthetic velocities were for an eddy with a Gaussian streamfunction which had peak velocity 0.25 units from its center. The eddy was centered either in the middle of the unit square or in the lower left hand corner. The eddy velocities varied as a sine wave within the single tidal cycle with a peak value of 1 velocity unit. 0.1 velocity units of normally distributed random noise were added to each component of the data, resulting in a velocity noise level of 14%. Tests compared the performance of the RBF tidal analysis using between 0 and 60 centers. The performance measure used in all but the cross validation technique was the RMS difference between the noiseless velocity of the underlying Gaussian eddy and the velocity predicted by the tidal RBF at 0.1 tidal cycle intervals at grid points spaced 0.05 units apart. To assess the variability in the RMS difference due to noise in the data each synthetic test case was repeated 50 times. The measure of variability used was the interval between the 5% and 95% percentile RMS differences for the 50 replicates, which will be referred to as the Replication Variability Interval (RVI).

3.2. Center Locations-greedy fit

Candela et al. [1992] and *Muenchow* [2000] subjectively placed their centers, while *Vennell* [2006] placed centers at 60m intervals along the vessel track. Tests with synthetic data are used to compare the performance of RBF tidal analysis for centers placed at random locations, at randomly selected data locations, evenly spaced along the vessel track,

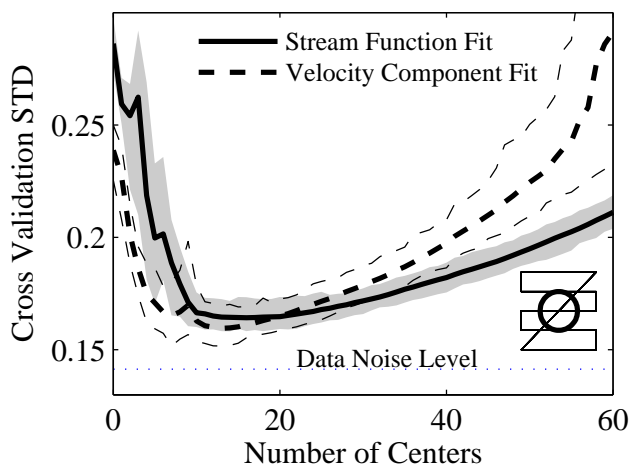


Figure 2. Cross validation curve to determine optimal number of centers for synthetic eddy. Plot gives standard deviation of the difference between predictions for the second half of the data and the measurements. Thick lines are averages for 50 randomly chosen “halves” for streamfunction fit (solid line) and velocity component fit (dashed). Gray area and thin dotted lines show the 5% and 95% percentiles of the STD for streamfunction and velocity component fits respectively for the 50 randomly chosen “halves”. Inset shows vessel track and eddy location.

on a grid and by the so called “greedy fit”. Fig. 1 compares the RMS difference between the synthetic eddy’s velocity and the tidal RBF velocity field for these five center placement schemes. The RMS differences for all schemes show a similar pattern. For low center numbers there is a rapid decrease in the RMS difference as additional centers give the surface more degrees of freedom to better fit the data. For large numbers of centers the difference increases as there are so many degrees of freedom that the RBF is fitting the noise in the data, i.e. over-fitting, which increases the difference between the fit and the underlying noiseless Gaussian eddy. The minimum in the curves at around 20-40 indicates an optimal number of centers, sufficient to adequately represent the eddy without over-fitting and reproducing the noise. At the minimum the RMS difference is only 4-8% of the peak velocity, less than the 14% noise level in the data.

The thin solid line in Fig. 1a shows the mean RMS difference between the fit and the eddy for 50 sets of randomly chosen center locations. The line demonstrates high RMS differences and high sensitivity to over-fitting. The thick dashed line in Fig. 1a shows the mean RMS difference for 50 sets of centers placed at randomly chosen data locations. It demonstrates significantly better performance than random locations, with a much lower RMS differences, low sensitivity to over-fitting and low RVI amongst the 50 sets (gray area). The open circles in Fig. 1b show the performance when placing centers at evenly spaced intervals along the vessel track and exhibits highly variable results and poor performance when over-fitting. The stars in Fig. 1b are for regular grids of centers, with equal numbers of centers in both the x and y directions, which perform poorly with the RMS difference for a 7 by 7 grid so large it is off scale. The tests in Fig. 1 confirm that placing centers at data locations gives on average better and/or less variable fits.

The thick solid line in Fig. 1a shows the performance of an iterative “greedy fit” technique which chooses a subset of data locations to be centers. The greedy fit starts by fitting just the polynomial part of (5) to the data. It then finds the data location with the largest residual between the initial surface and data and places the first center there. It then repeats this process, at each step fitting the data, then adding the data location with the largest residual to the growing set of centers. Placing a center at the data location with the largest residual does not guarantee the surface will pass through this data point. The idea behind the greedy strategy is to preferentially enhance the approximation power, or flexibility, of the RBF surface in the regions where it will be of greatest benefit. Typically these are regions of high curvature. Hence it is not surprising in Fig. 1a that the greedy fit can achieve a minimum RMS difference with fewer centers than the average for randomly chosen data locations. Consequently the greedy fit technique will be used for all subsequent fits.

3.3. Cross Validation Technique

A technique is needed to estimate the number of centers to best represent the velocity field without over-fitting and reproducing the noise. The comparison between the RBF fit and the underlying synthetic data in Fig. 1 showed that around 20-40 centers was optimal for this eddy. With real data sets a different technique is needed as there is no known underlying function with which to compare. The “cross validation” technique is a means of choosing the optimal number of parameters with which to fit a data set [*Felders*, 1999]. One form of the technique randomly chooses then fits half the data as a “training” data set and from this predicts values for the second half of the data. The difference between the predicted and measured second halves is used to determine the optimal number of fit parameters (for tidal RBFs

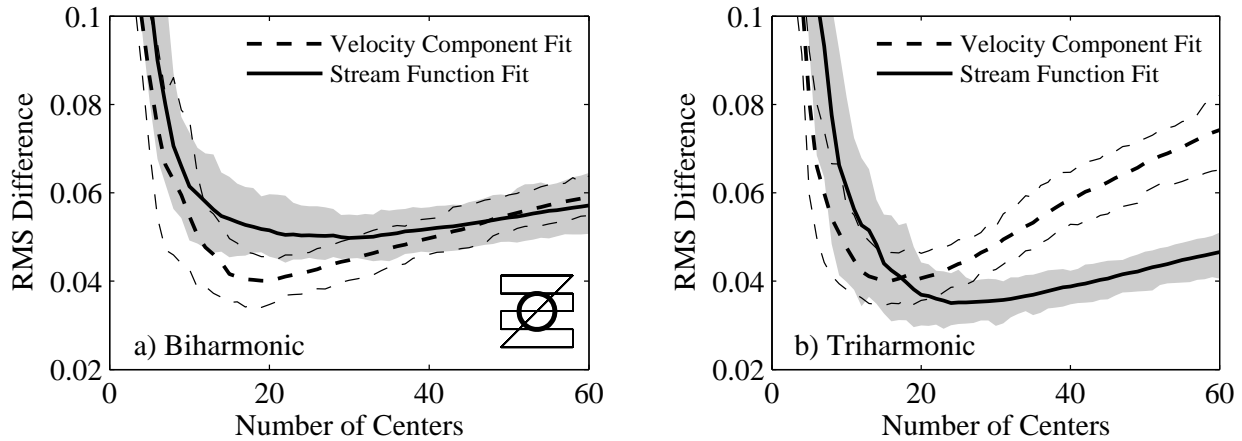


Figure 3. Comparison of fits to synthetic eddy using two TPS RBFs. Thick solid line is average RMS difference for streamfunction fit and thick dashed line is average difference for the velocity components fitted independently. Gray area and thin dotted lines show the RVI for the streamfunction and velocity component fits respectively based on 50 data sets. a) Biharmonic TPS. Inset shows vessel track and eddy location. b) Triharmonic TPS.

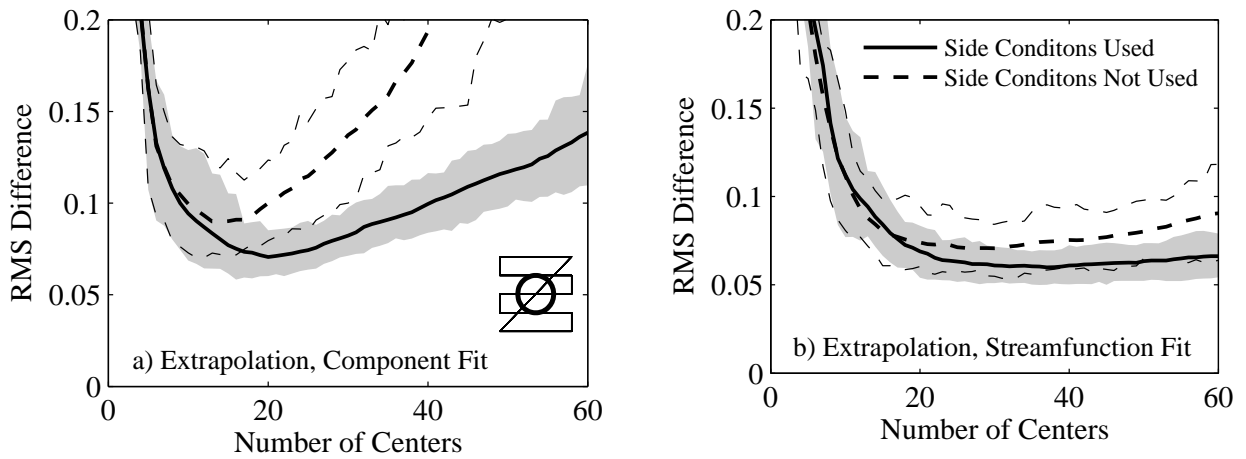


Figure 4. Effect of side conditions on triharmonic TPS RBF fits to synthetic eddy. Thick solid line is average RMS difference enforcing side conditions and thick dashed line is average difference without side conditions. Gray area and thin dotted lines show the RVI for fits with and without side conditions respectively based on 50 data sets. a) RMS difference for extrapolation of fit into a 0.1 wide strip around the measurement area for the velocity components fitted independently. b) RMS difference within extrapolated strip for streamfunction fit.

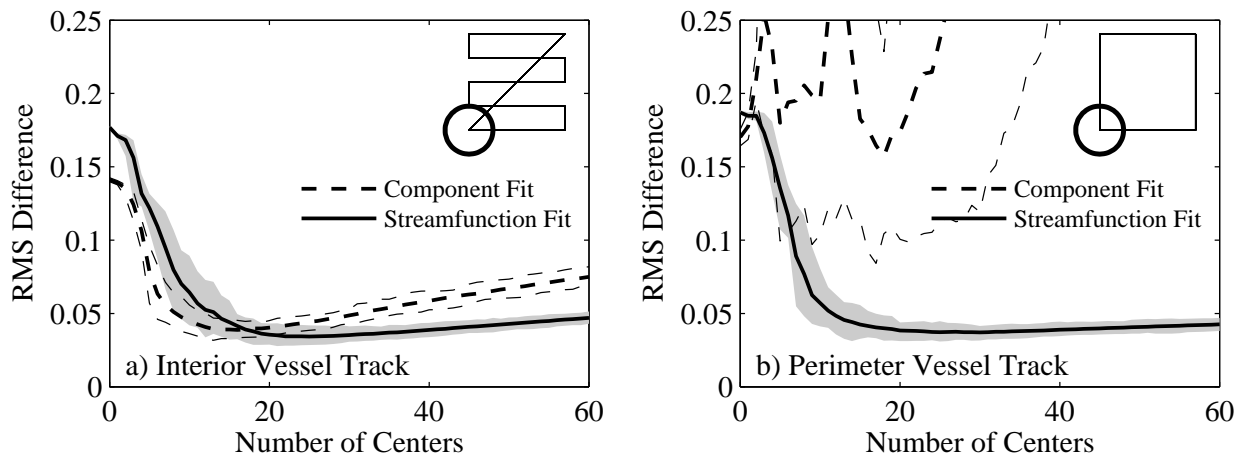


Figure 5. Performance of triharmonic TPS RBF fits for two vessel tracks. Thick solid line is average RMS difference using streamfunction fit and thick dashed line is average difference for velocity components fitted independently. Gray area and thin dotted lines show the RVI for streamfunction and component fits respectively based on 50 data sets. a) Vessel track with 5 lines through interior of unit square. b) Vessel track around perimeter of unit square. Velocity component fit is off scale for larger numbers of centers.

difference between the predictions for the second half of the measurements and the measured values. The plot exhibits a curve with a form similar to that in Fig. 1, for small numbers of centers adding centers improves the greedy fit, at high numbers there are too many degrees of freedom and the fit starts to reproduce the noise in the first half of the data. If the noise in the two halves is uncorrelated then the STD of the difference between the predictions and the measurements in the second half increases for large numbers of centers. The minimum in the STD plot indicates the optimal number of centers. To test the sensitivity to the data split the process is repeated for many randomly chosen “halves” of the data.

The thick dashed line in Fig. 2 gives the mean STD of the difference between predicted and measured second half for 50 random splits of the data. The line exhibits a minimum around 15-20 centers, sufficient to represent the eddy without over-fitting. With more data the minimum STD will converge on the noise level within the data and Fig. 2 confirms this where the minimum is around 16% slightly more than the 14% data noise.

4. Tidal Streamfunction Fit

The RBF tidal fit (5) is independently fitted to the components of the MV-ADCP measured velocities, however the components are physically related as they must satisfy mass continuity. For depth averaged flow mass continuity is

$$\frac{\partial \eta}{\partial t} + \frac{\partial}{\partial x}(u(h + \eta)) + \frac{\partial}{\partial y}(v(h + \eta)) = 0, \quad (7)$$

where η is the free surface displacement, h the water depth below mean sea level, u and v the components of depth averaged velocity. The ratio of magnitude of the first term relative to the others is $\frac{\omega \eta_0 L}{h_0 U_0}$, where ω is a representative tidal angular frequency, η_0 the surface tide’s amplitude, L the horizontal scale, h_0 a water depth and U_0 a horizontal velocity. For semi-diurnal tidal flow features of order 1km in size with $1m s^{-1}$ currents, in an area with 1m tidal amplitude and 10m water depths, this ratio is only 0.014. Thus for tidal features of the order of a few kilometers in size the first term in (7) can be neglected and the transport is approximately non-divergent. For repeated circuit MV-ADCP measurements vessel speeds are typically $8km hr^{-1}$ and circuits are completed hourly and consequently measurements are restricted to a 2km square, or smaller, area. Thus the transport of tidal flow features measured by this technique is typically non-divergent. When the first term of (7) can be neglected the transport streamfunction defined by

$$\frac{\partial \psi}{\partial y} = u(h + \eta), \quad \frac{\partial \psi}{\partial x} = -v(h + \eta) \quad (8)$$

satisfies mass continuity. The streamfunction can be expressed as a tidal RBF (15) or

$$\psi(\mathbf{x}, t) = F_0^\psi(\mathbf{x}) + \sum_{m=1}^M [F_m^\psi(\mathbf{x}) \cos(\omega_m t) + G_m^\psi(\mathbf{x}) \sin(\omega_m t)], \quad (9)$$

where each of the F^ψ ’s and G^ψ ’s are RBFs of the form (2). Again these RBFs are of identical form as they use the same centers. They differ only in the values of their coefficients. We can exploit the differentiability of the RBF representation to fit the transport streamfunction directly to the MV-ADCP measurements using a modified form of (4). For steady flows this is done by obtaining the least squares solution to a set of equations evaluating (8) at the

data locations,

$$\begin{bmatrix} \frac{\partial \mathbf{A}}{\partial y} & \frac{\partial \mathbf{P}}{\partial y} \\ \frac{\partial \mathbf{A}}{\partial x} & \frac{\partial \mathbf{P}}{\partial x} \end{bmatrix} \mathbf{w}^\psi \approx \begin{bmatrix} u(h + \eta) \\ -v(h + \eta) \end{bmatrix} \quad (10)$$

which is solved subject to the side conditions (3) applied to λ^ψ . The elements in the streamfunction design matrix in (10) are evaluated from the analytic spatial derivatives of the RBF. As before, the extension from steady flow to tidal current design matrix is straight forward, augmenting both \mathbf{A} and \mathbf{P} on the right with $2M$ copies of themselves multiplied by either a $\sin(\omega_m t)$ or a $\cos(\omega_m t)$. In solving for the coefficients of the tidal streamfunction, there is an function of time only which cannot be determined. However this function has zero spatial derivatives and thus yields no velocities and can be set after streamfunction evaluation, e.g. chosen so that the streamfunction is zero at the coast.

The components of transport can be calculated from the analytic spatial derivatives of (9). To obtain tidal velocities we also need the instantaneous total depth, $\eta + h$. This could be obtained from a tidal RBF of the form (9) fitted to the instantaneous ADCP measured water depth. However, attempting this with the field data presented later gave unrealistic 0.5m differences in instantaneous water level across an area with 10m depths and a 2m tidal range. One alternative is to use surface heights from a nearby tide gauge. The surface tide can be decomposed into the height at the gauge plus a dynamic component i.e. $\eta(\mathbf{x}, t) = \eta_T(t) + \eta_D(\mathbf{x}, t)$. The instantaneous variation in water level, η_D , over a few kilometers is typically only a few centimeters [Vennell, 2006], compared to tidal amplitudes of $O(1m)$. Thus $\eta(\mathbf{x}, t)$ can be approximated by $\eta_T(t)$, which can be predicted from the tidal coefficients for the gauge (this approximation for $\eta + h$ is improved if $|\eta| \ll h$). The depth below mean sea level h can be found by subtracting the tide gauge’s water level from the raw ADCP measured depths. h can be fitted with a time invariant RBF (2) to give the coefficients \mathbf{w}^h , which can be used to give the bathymetry at any location. Tidal velocities at any location or time can be calculated from the gauge’s tidal coefficients, together with the RBF representation of h and the analytic spatial derivatives of the RBF representation of ψ . Velocity gradients can be evaluated from the analytical first and second derivatives of the streamfunction and bathymetry RBFs. To ensure continuity of the second derivative, tri-harmonic TPS are used. In this case the polynomial P is quadratic.

4.1. Coastal Constraints

MV-ADCP measurements are often made near coastlines and the RBF streamfunction formulation makes it easy to constrain the velocity field to be parallel to the coast. This is done by requiring the tidal streamfunction coefficients evaluated at the coastal locations to have the same value as at the first point in a coastal segment. This can be expressed as a set of equations

$$\begin{aligned} F_0^\psi(\mathbf{x}_j^b) - F_0^\psi(\mathbf{x}_1^b) &= 0, \\ F_m^\psi(\mathbf{x}_j^b) - F_m^\psi(\mathbf{x}_1^b) &= 0, \\ G_m^\psi(\mathbf{x}_j^b) - G_m^\psi(\mathbf{x}_1^b) &= 0, \end{aligned} \quad \text{for } j = 2, \dots, N_b \quad (11)$$

where \mathbf{x}_j^b are the locations of the N_b coastal constraint points in the segment and the constraints are imposed separately for each frequency. Each equality in (11) is the difference of two RBFs. Although evaluated at different locations they contain the same RBF coefficients. Thus each of the $2M + 1$ equalities in (11) is a set of $(N_b - 1)$ equations which force these corresponding RBF coefficients to be related in such a

way that the streamfunction has the same value all along the coastal segment. The coastal constraints (11) specify only direction, not the magnitude of the velocity at the coast, thus implicitly require extrapolation of the streamfunction to the coast. Consequently the side conditions (3), are necessary to improve this extrapolation. The coastal constraints augment the side conditions (3) and (10) is solved subject to an expanded set of linear equality constraints. To prevent the constraints significantly affecting the fit within the measurement area it was found necessary to include the coastal locations as centers, which provided additional spatial resolution in order to accommodate the constraint. Synthetic tests (not shown) indicated that the coastal constraint had little effect, only slightly improving the directions of RBF tidal velocities near the coast.

4.2. Performance of Streamfunction Fit

The solid line in Fig. 2 is the cross validation curve for the streamfunction fit (9) to the Gaussian eddy. The streamfunction fit has a similar minimum to that when fitting the velocity components independently (5), but smaller RMS differences when over-fitting. Fig. 3a shows that with biharmonic TPS the velocity component fit does slightly better than the streamfunction fit at the RMS minimum with very similar RVI at larger numbers of centers. When fitted using triharmonic TPS, Fig. 3b, both component and streamfunction fits show lower RMS differences and while they have a similar minimum, the streamfunction fit performs much better when over-fitting than the component fit and has a smaller RVI. The stream function is found by fitting derivatives of the RBF (5) to noisy data. This differentiation amplifies noise in the data. However using the smoother triharmonic TPS reduces the additional noise in the fit sufficiently for the streamfunction to out perform the component fit when over-fitting. Consequently, we will use triharmonic TPS for all subsequent fits.

RMS plots (not shown) demonstrate that enforcement of the side conditions slightly reduces the RMS difference within the measurement area and its variability, particularly when over-fitting. Fits may be required to be extrapolated slightly outside the measurement area and Fig. 4a compares RMS difference for the component fit in a 0.1 unit wide strip surrounding the measurement area. In this extrapolated area TPS are prone to bend rapidly upwards or downwards. The side conditions (3) constrain the far field behavior of triharmonic TPS to be quadratic in distance from the measurements. Fig. 4a demonstrates that the side conditions significantly improve the component fit within the extrapolated area, particularly when over-fitting. Fig. 4b demonstrates that the extrapolated streamfunction performs better than the component fit, and enforcing the side conditions gives a further slight improvement.

A major advantage of TPS is their ability to smoothly span large gaps in the data. This was tested by placing a Gaussian Eddy in the lower left corner of the measurement area and comparing the performance for two vessel tracks. One track, as used previously, with five lines across the interior of the unit square measurement area and the other with ADCP measurements around the perimeter of the measurement area. Fig. 5 compares the RMS differences for predictions based on the same number of measurements on a 0.05 unit grid inside the area bounded by the vessel track. For the 5 line vessel track, Fig. 5a, the RMS differences for the component and streamfunction triharmonic fits are similar to those for the centrally located eddy in Fig. 3b, with the streamfunction fit performing better when over-fitting and exhibiting lower RVI amongst the 50 data sets. For a perimeter vessel track the component fit is almost incapable of representing the eddy, with very large RMS differences

> 0.2 and highly variable results as indicated by large RVI. Remarkably the streamfunction fit for a perimeter vessel track, Fig. 5b performs almost as well as that when the vessel traverses the interior, clearly resolving the eddy from a less than ideal data set. Thus imposing mass continuity by use of the streamfunction fit can significantly improve the ability of TPS to span large gaps in the vessel track.

Fig. 6 compares the simpler box binning technique used by *Geyer and Signell* [1990] and others with the RBF technique. The box binning of the data was done by breaking the 0.2 unit spaced vessel tracks into equal length horizontal bins. The data in each bin was fitted with sinusoids using conventional tidal analysis *Godin* [1972]. Tidal predictions based on the binned tidal analysis were linearly interpolated to the 0.05 unit fine grid for comparison with the underlying Gaussian eddy. Fig. 6a shows that the box binned fits has a minimum RMS difference around 70 bins of 0.1 velocity units. The triharmonic streamfunction fit has a minimum RMS difference of only 0.04 units, demonstrating the advantage of the smoother streamfunction technique. In addition the binned fit curve in Fig. 6a exhibits slightly erratic behavior as more bins are added despite being the average RMS difference of 50 trials. In contrast the RBF fits behave relative smoothly as centers are added. The RBF velocity component fit also exhibits a much lower RMS difference than the binned fit. The advantage of the RBF fits was found to be greater for wider spaced vessel tracks.

Fig. 6b compares the vorticity calculated from the three types of fit. Vorticity for the streamfunction and component RBF fits were calculated from the analytic derivatives of their RBF representation. Vorticity for the binned fit was calculated using centered finite differences of the 0.05 unit interpolated grid velocity values. The minimum RMS difference for the streamfunction and component RBF fits are nearly half the size of the minimum binned fit difference, indicating the advantage of the RBF fits in extracting the vorticity from noisy velocity measurements.

5. Field Data

Bluff Inlet, in southern New Zealand, is dominated by semidiurnal tides with a $55km^2$ area at spring high tide and $22km^2$ at low tide. During spring tides $97 \times 10^6 m^3$ of water is exchanged through its narrow entrance channel with the Pacific Ocean [*Heath*, 1976]. MV-ADCP measurements were made in February 1998 within Bluff Harbour, which is immediately inside the entrance to the Inlet, Fig. 7. To assist presentation all figures are rotated 40° anticlockwise from true north, but for convenience we will refer to the top and right of the figures as “north” and “east”. The flood tide enters the Harbour from the east through a 10m deep entrance channel, with as little as 100m between the 5m contours. Peak flows in the narrowest section are $2.5ms^{-1}$ reducing to $1.6ms^{-1}$ on the eastern edge of the measurement area. The flood flow forms a narrow jet, with a counter clockwise eddy forming to the south of the jet, Fig. 8. Erosion by the flood jet is responsible for the deep water off Tiwai Wharf and within the blind channel, as well as the flood tidal delta formed from the deposition of its sediment load. The weaker eastward ebb flows occur around the southern side of the delta through the ebb channel. In this work we focus on the flood tidal jet and eddy.

The vessel measurement track covered the area between Island Harbour, Tiwai Wharf and Town Wharf, which is mostly dredged to a depth of 9m, Fig. 7. The $8km$ long track was completed hourly for 13 hours at an average vessel speed of $2ms^{-1}$. The track, which began at Town Wharf traveling west, consisted of a series of lines across and along channel chosen to maximize the area covered, while resolving the important features. The measurements were made with a 600kHz RDI Broadband ADCP recording currents in 1m depth intervals averaged over 8.5sec ensembles spaced

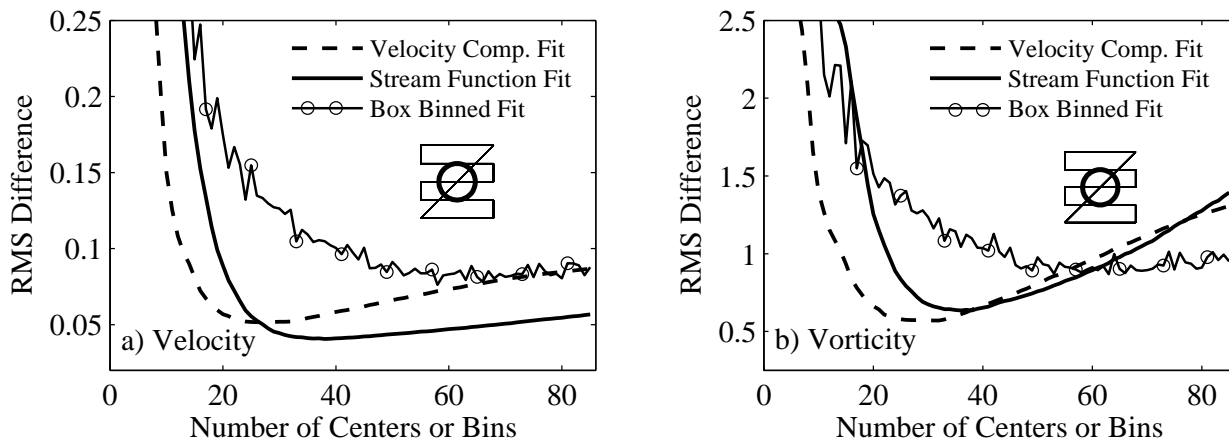


Figure 6. Comparison of tidal RBF fits and box binning technique. Thick solid line is average RMS velocity difference with synthetic eddy using a streamfunction fit, the thick dashed line is average difference for velocity components independently fitted with a tidal RBF and the solid line with circles the differences for velocity data horizontally binned and fitted using conventional tidal analysis. a) RMS velocity difference between the fit and underlying Gaussian eddy. b) RMS difference between vorticity calculated from the fits and the vorticity of the underlying Gaussian eddy.

10m-30m apart. The velocities were depth averaged assuming no shear above the upper most depth bin at 2.9m and a logarithmic velocity profile between the deepest good depth bin and the ADCP measured water depth. There were 5832 ensembles in the 13 hour data sets and Fig. 8 gives an example of raw data from one circuit during the flood which clearly shows the flood jet in the north and the associated eddy to the south.

A tidal streamfunction RBF (9) with quadratic polynomial was fitted to the ADCP measured transports. Tidal frequencies of M2, M4 and M6 were used as representative of the major tidal frequency bands resolvable from the 13 hours of data. The 5832 transports were randomly divided into training and validation halves. The training half was fitted with a triharmonic TPS RBF using a greedy fit with up to 100 centers with quadratic polynomial. The fit was repeated for 50 randomly chosen “halves”. The STD of the differences between the predictions for validation half and measured values gave a curve (not shown) similar to that in Fig. 2 with a minimum around 60 centers. The minimum transport STD was $1.4m^2s^{-1}$, which for a typical 10m depth indicates that the velocity not explained by the tidal RBF was around $0.14ms^{-1}$, a value small compared to the $1.6ms^{-1}$ peak flows. A greedy fit was then made to all the measured transports with 60 centers, enforcing equal streamfunction at 13 locations along the 11m vertical wall of the Island Harbour berths. With 60 centers, 6 polynomial terms and 3 frequencies the fit’s design matrix \mathbf{D}^{tidal} was 5832 by 462. The locations of the centers are given in Fig. 8 and exhibit higher densities in areas where the velocity has greater horizontal variation.

The tidal predictions for the gauge at Island Harbour were used to reduce the MV-ADCP measured depths to a depth below gauge datum. These reduced depths were fitted with a time invariant RBF (2) using a greedy fit with 60 centers. The gauge’s tidal coefficients, the depth below datum RBF and the tidal streamfunction RBF were then used to predict the streamfunction, velocities and vorticity which are shown in Fig. 9.

5.1. Eddy Structure and Development

Fig. 9a gives the streamfunction and velocities when the eddy first forms at HW-04:45. The thick line is the contour corresponding to the coastal streamfunction value, which first stagnates on Island Harbour at this time. The stagnation streamline originates in the east at the location of the

maximum vorticity in the flood tidal jet, i.e. the point of inflection in the jet’s cross channel velocity profile. This inflection is shown by the thick dashed gray line which shows that the highest vorticity fluid in the jet is contributing to the eddy’s growth. The rotated numbers on the east give the maximum vorticity and velocity on the eastern boundary. At this time the jet’s peak flow is $0.6ms^{-1}$ and the maximum vorticity $70 \times 10^{-4}s^{-1}$, 1-2 orders of magnitude larger than planetary vorticity. At HW-03:00, Fig. 9b, the eddy’s transport, given by the maximum streamfunction is $500m^3s^{-1}$ at a time when the jet is an order of magnitude larger, $4500m^3s^{-1}$. The stagnation streamline now originates 100m south of the jet’s vorticity maximum of $106 \times 10^{-4}s^{-1}$ and jet’s peak velocity has increased to $1.5ms^{-1}$. By HW-02:15, Fig. 9c, the stagnation streamline no longer intersects the eastern boundary as the eddy became isolated from its fluid source around HW-02:30. On the eddy’s western side the stagnation point lies close to tip of Island Harbour throughout the period HW-04:45 to HW-01:30, e.g. Fig. 9b.

The eddy’s structure is clearly seen in the tracks of drogues advected by the velocities predicted by the tidal streamfunction RBF fit in Fig. 10. These virtual drogues released at HW-03:00 have different fates depending on whether they are released north or south of the point where the stagnation streamline intersects the eastern boundary, Fig. 9b. The drogues released to the north, $\psi < 0$, rapidly traverse the measurement area in 20min as part of the jet. The drogues released at $\psi = 0$ and $\psi = 150$, become part of the eddy, persisting within it for more than 3 hours. The drogue released at the stagnation streamline does not hit the coast as the streamlines are unsteady. The drogue released at $\psi = 150$ remains closer to the eddy’s center than that released at $\psi = 0$, demonstrating that the eddy grows in spiral fashion, with fluid originating near the stagnation streamline forming the outer layers. The eddy completes around one full rotation of the spiral during its life.

More details of the eddy’s and jet’s developments can be seen in time series of their transport Fig. 11a. The eddy’s transport is the maximum value of ψ in Fig. 9 and the jet’s transport was taken as twice the value of ψ at the jet’s center on the eastern boundary. In Fig. 11a the eddy’s transport is an order of magnitude smaller than the jet’s, and the eddy’s transport peaks around HW-02:45, prior to the time the eddy becomes isolated from the jet. The jet’s transport peaks a hour later, at HW-01:45. The eddy’s mean vorticity

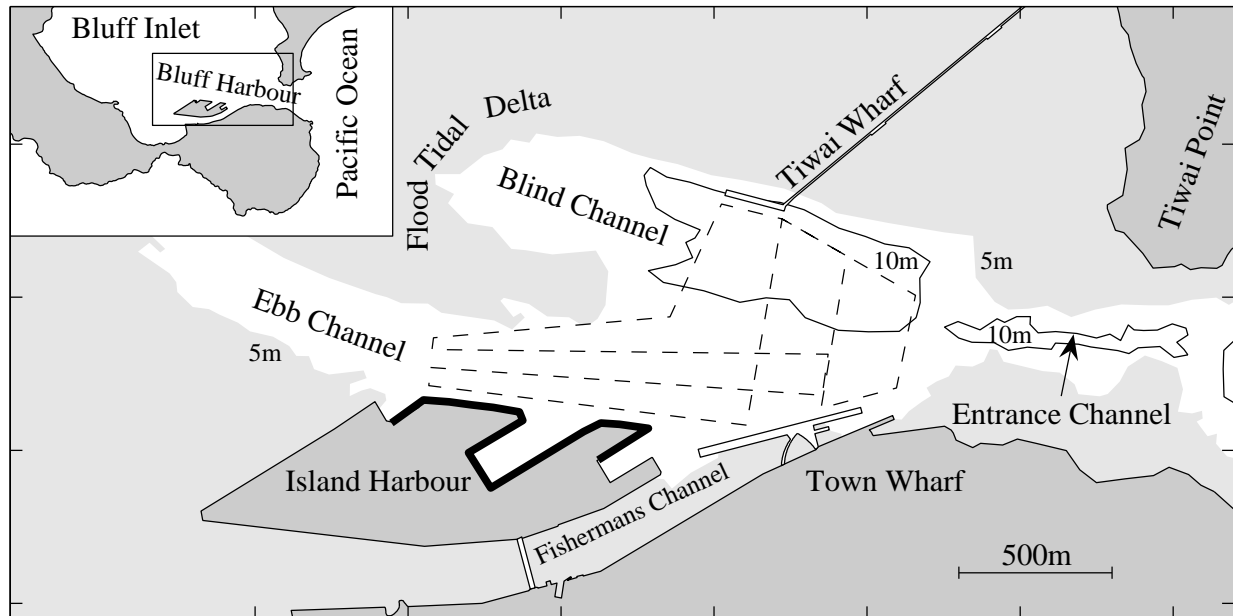


Figure 7. Bluff Harbour at the southern end of NZ's South Island. Harbour entrance is on the eastern side and thin dashed line shows the vessel track. Thick solid line indicates where coastal constraints are enforced on tidal streamfunction RBF fit. Light gray areas have depths less than 5m.

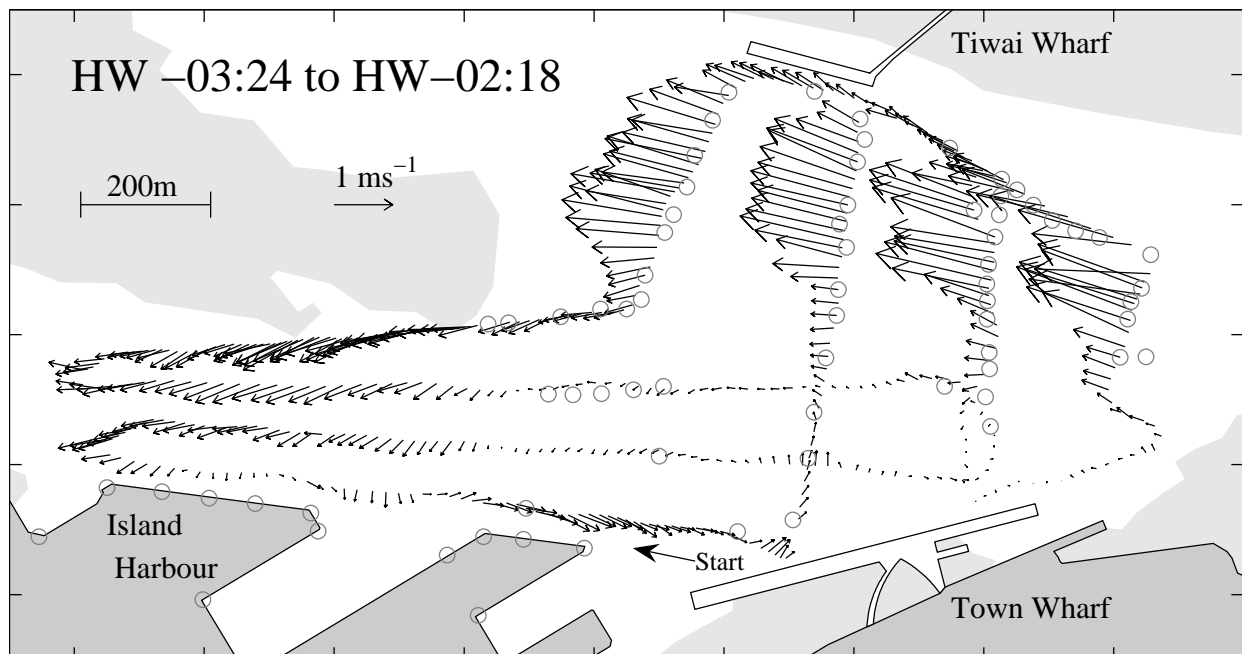


Figure 8. One hour sample of depth averaged MV-ADCP velocity data showing flood tidal jet and eddy. Vessel track began at Town Wharf heading west. Gray circles show locations of centers of RBF chosen by the “greedy fit” technique, together with those at the coastal constraint locations.

was estimated by predicting the vorticity on a 10m grid and then averaging those where ψ was greater than its coastal value. The time series of eddy vorticity in Fig. 11b exhibits a peak around HW-03:00, slightly ahead of the time the eddy becomes isolated. The eddy's vorticity grows as it is fed from the jet, but is also dissipated by bottom and lateral friction. At the time the eddy's vorticity peaks dissipation balances input from the jet. After this time dissipation exceeds input, leading to a decline of eddy vorticity which continues after the eddy is isolated from the jet source. The jet's and

eddy's maximum vorticities are plotted Fig. 11b and show that, when the eddy is first formed at HW-04:45, the eddy is fed fluid from the jet's vorticity maximum, Fig. 9a. As the entry point of the stagnation streamline moves southward, the maximum vorticity of fluid entering the eddy declines until the eddy becomes isolated.

Wells and van Heijst [2003] discuss the dipole eddies formed downstream of a narrow inlet connecting an embayment to the ocean. They noted that if $W/UT < 0.13$, (where W is the inlet width, U the flow velocity and T the tidal period) that the eddies can propagate away from the inlet after

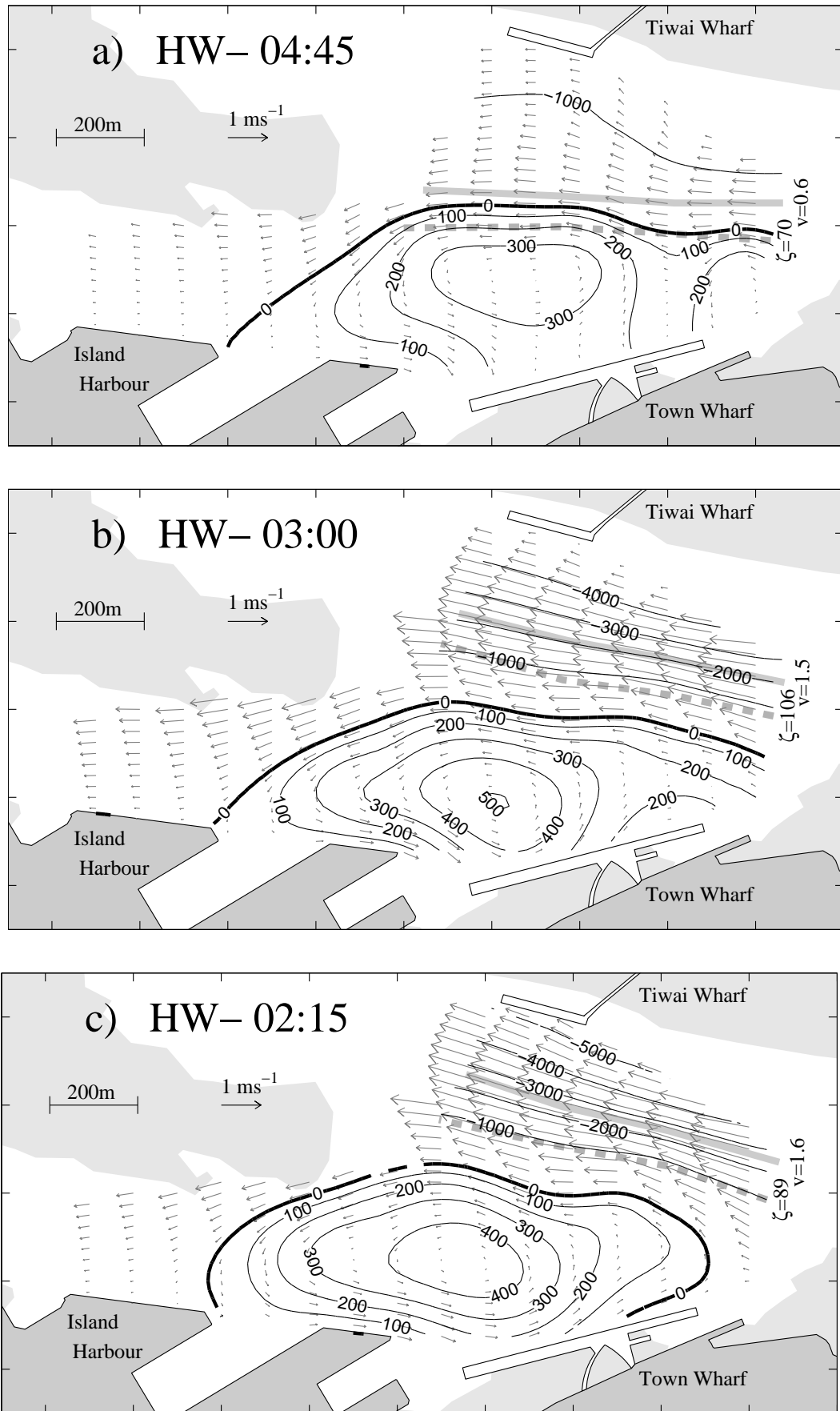


Figure 9. MV-ADCP measurements of tidal streamfunction. Contours give streamfunction in $m^2 s^{-1}$ relative to the value at Island Harbour coastal constraint. Thick dark contour is the stagnation streamfunction. Light gray areas have depths less than 5m. Thick gray solid line gives axis of flood tidal jet. Thick gray dashed line is location of southern vorticity maximum within the jet. Rotated numbers on eastern side give jet's maximum velocity, v , in ms^{-1} and vorticity, ζ , in $10^{-4} s^{-1}$ at its entry into the measurement area. a) HW-04:45. b) HW-03:00. c) HW-02:15.

ter high water. The ADCP measurements confirm this, with the eddy persisting within the measurement area near the Harbour entrance up to the time the ebb flow begins, presumably being advected out of the Harbour some time after high tide. *Hench and Luettich* [2003] model tidal exchange through inlets observing dipole residual flows on both sides of the inlet as the result of eddy pairs form down stream of the inlet on both phases of the tide. The Bluff flood tidal eddy results in strong eastward residual flows (estimated from the time invariant part of the tidal RBF (9)) of up to $0.3ms^{-1}$ in the south of the measurement area area.

6. Conclusions

The major advantage of TPS RBFs is their ability to interpolate smoothly across large gaps in irregularly spaced measurements. Fig. 6 demonstrates the advantage of these smoother RBF fits over the simpler box binning technique in extracting velocity and vorticity from noisy ADCP measurements. Interpolation theory shows that when the surface passes through every data point then the uniquely smoothest interpolant for a measure of energy of the form (1) is an RBF (2) with the centers at every data location and weights which satisfy the side conditions (3). The tests with synthetic data demonstrate that, when seeking a smoother surface with fewer centers than data, enforcing these conditions on a least squares RBF can significantly improve the fit. Fig. 1 demonstrates that simply moving centers to data locations can significantly lower average RMS difference and/or lower noise induced variability when compared to locating centers arbitrarily or evenly spaced along the vessel track as previous oceanographic works have done. Enforcing the side conditions (3) on the least squares fit also improves the fit as confirmed by test results in Fig. 4 where their use lowers the RMS difference particularly when over-fitting. Lower RMS differences when over-fitting gives a more robust fit, less sensitive to the choice of the optimal number of centers. The side conditions constrain the far field behavior of the RBF which tests demonstrate significantly improves performance when extrapolating slightly outside the measurement area, Fig. 4a. The greedy fit technique is a computationally efficient way to select a subset of data locations to be centers. Cross validation provides a technique to determine the optimal number of centers, sufficient to represent the velocity structure without over-fitting. Higher order TPS RBFs, such as the triharmonic, have continuity of higher order derivatives and give a smoother fit. The RBF representation allows analytic evaluation of velocity gradients from the fit which can be used to provide observations of quantities such as vorticity.

For tidal flows with scales less than a few kilometers the differentiability of the RBF can be exploited to fit the tidal streamfunction to MV-ADCP measured transports. This can significantly improve the ability of the RBF to represent the tidal velocity field by constraining the velocity components to satisfy mass continuity. In particular the streamfunction approach improves the ability of the RBF to span large gaps between vessel tracks; Fig. 5b demonstrated that the streamfunction fit was able to resolve velocities within a unit square from measurements made on vessel track which traversed the edges of the square almost as well as a vessel track with 5 lines through the interior of the square. Coastal constraints on the streamfunction fit marginally improve the fit, but more usefully give the coastal streamfunction value which can be used to clearly identify stagnation streamlines which delineate tidal flow structures. In almost all tests the streamfunction fit (9) performed better than the component fit (5), however improvements by placing centers at data locations and enforcing the side conditions when using

the streamfunction fit were proportionately less than when fitting the components independently. The streamfunction RBF technique is limited to scales of a few km or less, but there are many tidal jets, channel flows and flow separations of this scale and smaller in the coastal ocean for which the technique could provide exceptionally detailed flow observations. On larger scales the presented improvements to *Candela et al.*'s velocity component fit can yield high quality observations.

The ADCP measurements from Bluff Harbour show an eddy which forms around HW-04:45 and is fed fluid and vorticity from the flood tidal jet inshore of the jet's vorticity maximum. The eddy grows in a spiral fashion completing around one turn in its life time. The lateral extent within the jet from which the eddy derives its fluid decreases progressively from its formation until it becomes isolated around HW-02:20. Throughout the eddy's life the jet's axis rotates clockwise with time. The reason for the jet's rotation is unclear, as is the role of jet rotation in isolating the eddy. However the tidal RBF streamfunction analysis has provided extraordinarily detailed velocity observations which provide the basis for models to fully understand the evolution of the eddy and jet.

Acknowledgments. Southport, NZ Ltd for the use of the ADCP data

7. Appendix

To facilitate implementing the RBF tidal analysis technique the detailed structures of the matrices are given below for a 2D RBF with linear supplemental polynomial. The least squares problem which must be solved to find the RBF weights and polynomial coefficients is (4) or

$$\begin{bmatrix} \Phi_{11} & \dots & \Phi_{1N} & 1 & x_1^d & y_1^d \\ \Phi_{21} & \dots & \Phi_{2N} & 1 & x_2^d & y_2^d \\ \Phi_{31} & \dots & \Phi_{3N} & 1 & x_3^d & y_3^d \\ \vdots & \vdots & \vdots & \vdots & \vdots & \vdots \\ \Phi_{L1} & \dots & \Phi_{LN} & 1 & x_L^d & y_L^d \end{bmatrix} \begin{bmatrix} \lambda_1 \\ \lambda_2 \\ \vdots \\ \lambda_N \\ \beta_1 \\ \beta_2 \\ \beta_3 \end{bmatrix} = \begin{bmatrix} d_1 \\ d_2 \\ d_3 \\ d_4 \\ d_5 \\ \vdots \\ d_L \end{bmatrix} \quad (12)$$

where $\Phi_{ij} = \Phi(|\mathbf{x}_i^d - \mathbf{y}_j|)$, \mathbf{x}_i^d is the position vector of the i th data point and x_i^d and y_i^d are its components. Similarly \mathbf{y}_j is the position vector of the j th RBF center. λ_j is the weight for the function $\Phi(|\mathbf{x} - \mathbf{y}_j|)$ and the β_j 's are the coefficients of the linear polynomial with respect to the basis $\{1, x, y\}$. The d_j 's are the measured surface heights. Equation (12) is solved subject to the side conditions (3), which expressed are expressed in matrix form as

$$\begin{bmatrix} 1 & 1 & \dots & 1 \\ x_1^c & x_2^c & \dots & x_N^c \\ y_1^c & y_2^c & \dots & y_N^c \end{bmatrix} \begin{bmatrix} \lambda_1 \\ \lambda_2 \\ \vdots \\ \lambda_N \end{bmatrix} = \begin{bmatrix} 0 \\ 0 \\ 0 \end{bmatrix} \quad (13)$$

where x_j^c and y_j^c are the components of \mathbf{y}_j . Once the λ_j 's and β_j 's are found by solving (12) the surface height can be evaluated using (2) which can be expressed in indicial notation as

$$F(\mathbf{x}) = \beta_1 + \beta_2 x + \beta_2 y + \sum_{j=1}^N \lambda_j \Phi(|\mathbf{x} - \mathbf{y}_j|) \quad (14)$$

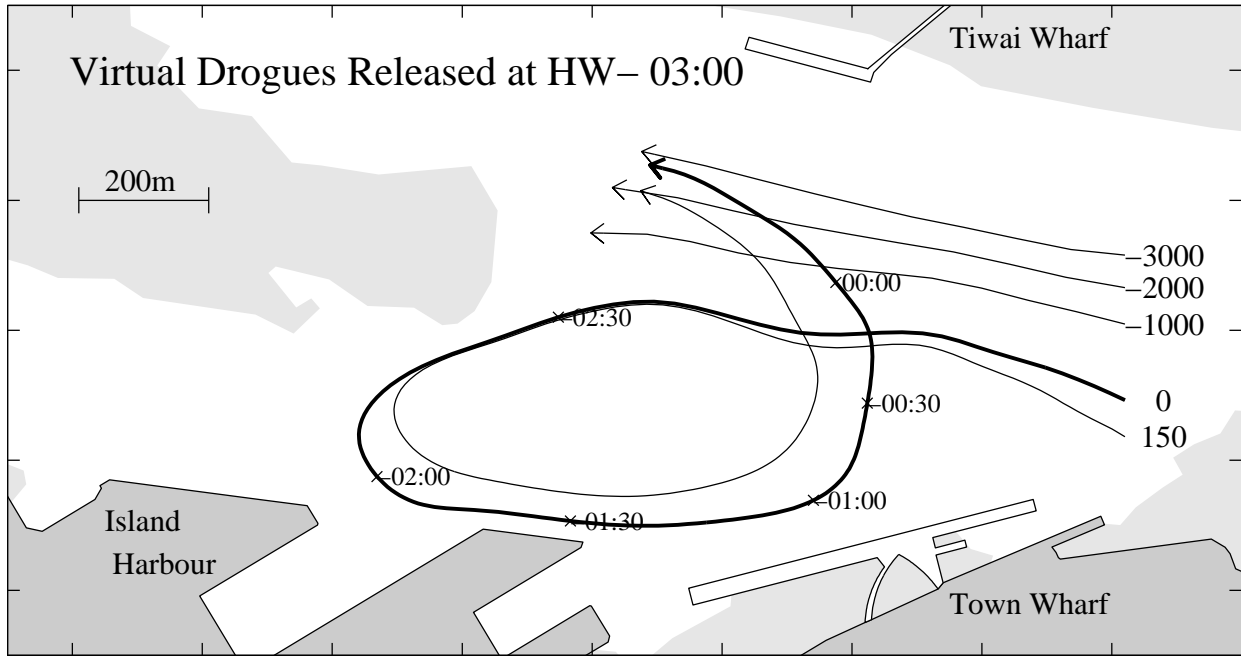


Figure 10. Tracks of virtual drogues advected by predicted tidal streamfunction velocities. Drogues were released on eastern boundary at HW-03:00. Numbers near release point are the streamfunction value at release. Thick solid line is drogue released at the entry point of stagnation streamline and crosses show locations of this drogue at given times.

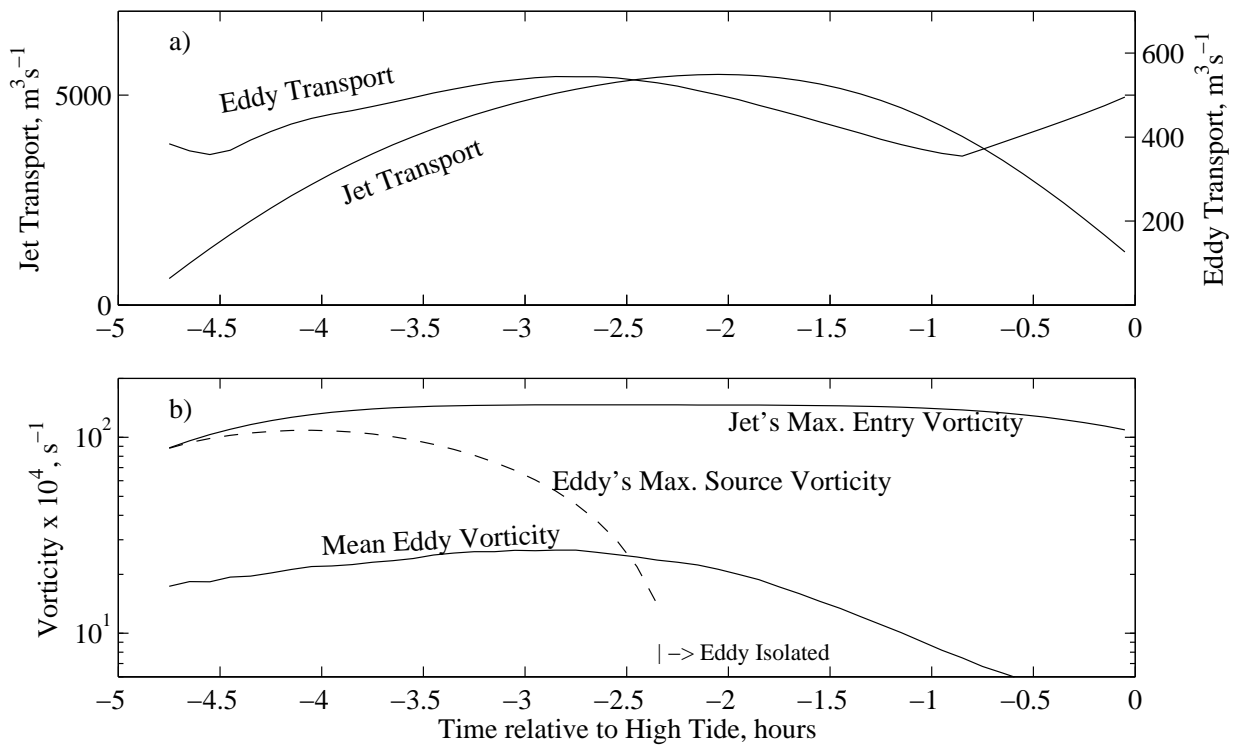


Figure 11. Time series of eddy and jet development. a) Transport, note different scales. b) Vorticity, log scale. Upper solid line is jet's maximum vorticity at entry to measurement area. Lower solid line is eddy's average vorticity and dashed line is the maximum vorticity of fluid entering the eddy across the eastern boundary. After HW-02:20 eddy is isolated from its jet source.

The tidal RBF velocity representation used in (5) and (9) can be written in indicial form as

$$\begin{aligned}
 F(\mathbf{x}, t) = & \left\{ \beta_{01} + \beta_{02}x + \beta_{03}y + \sum_{j=1}^N \lambda_{0j} \Phi(|\mathbf{x} - \mathbf{y}_j|) \right\} \\
 & + \sum_{m=1}^M \left\{ \beta_{Cm1} + \beta_{Cm2}x + \beta_{Cm3}y \right. \\
 & \quad \left. + \sum_{j=1}^N \lambda_{Cmj} \Phi(|\mathbf{x} - \mathbf{y}_j|) \right\} \cos(\omega_m t) \\
 & + \sum_{m=1}^M \left\{ \beta_{Sm1} + \beta_{Sm2}x + \beta_{Sm3}y \right. \\
 & \quad \left. + \sum_{j=1}^N \lambda_{Smj} \Phi(|\mathbf{x} - \mathbf{y}_j|) \right\} \sin(\omega_m t). \quad (15)
 \end{aligned}$$

References

- Beatson, R. K., J. B. Cherrie, T. J. McLennan, T. J. Mitchell, J. C. Carr, W. R. Fright, and B. C. McCallum, Surface reconstruction via smoothest restricted range approximation, in *Geometric modeling and computing*, edited by M. L. Lucian and M. Neamtu, pp. 41–52, Nashboro Press, 2004.
- Bjorck, A., *Numerical Methods for Least Squares*, SIAM, 1996.
- Candela, J., R. C. Beardsley, and R. Limburner, Separation of tides and sub-tidal currents in ship-mounted ADCP observations, *Journal of Geophysical Research*, *97*, 769–788, 1992.
- Felders, A., Statistical concepts, in *Intelligent Data Analysis*, edited by M. Bethold and D. Hand, pp. 15–66, Springer, 1999.
- Geyer, W. R., and R. P. Signell, Measurements of tidal flow around a headland with a shipboard ADCP, *Journal of Geophysical Research*, *95*, 3189–3197, 1990.
- Godin, G., *The Analysis of Tides*, Liverpool, 1972.
- Heath, R., Broad classification of New Zealand inlets with emphasis on residence times, *N.Z. Journal of Marine and Freshwater Research*, *10*, 429–444, 1976.
- Hench, J., and R. Luettich, Transient tidal circulation and momentum balances at a shallow inlet, *Journal of Physical Oceanography*, *33*, 913–932, 2003.
- Meinguet, J., Multivariate interpolation at arbitrary points made simple, *Zeitschrift für Angewandte Mathematik und Physik*, *30*, 292–304, 1979.
- Muenchow, A., Detiding three-dimensional velocity data in coastal waters, *Journal Atmospheric and Oceanic Technology*, *17*, 736–748, 2000.
- Old, C. P., and R. Vennell, ADCP measurements of the velocity field of an ebb tidal jet, *Journal of Geophysical Research*, *106*, 7037–7050, 2001.
- Simpson, J., E. Mitchelson-Jacob, and A.E.Hill, Flow structure in a channel from an ADCP, *Continental Shelf Research*, *10*, 589–603, 1990.
- Vennell, R., ADCP measurements of tidal phase and amplitude in Cook Strait, New Zealand, *Continental Shelf Research*, *14*, 353–364, 1994.
- Vennell, R., ADCP measurements of momentum balance and dynamic topography in a constricted tidal channel, *Journal of Physical Oceanography*, *36*, 177–188, 2006.
- Wells, M., and G. van Heijst, A model of tidal flushing of an estuary by dipole formation, *Dynamics of the atmosphere and oceans*, *37*, 223–244, 2003.

R. Vennell, Department of Marine Science, University of Otago, 310 Castle St, Dunedin, NZ (rvennell@otago.ac.nz)

R. Beatson, Department of Mathematics, University of Canterbury, Christchurch, NZ (rick.beatson@canterbury.ac.nz)